Influence of Mg^{2+} on the conformational flexibility of a tetracycline aptamer

THILO HETZKE,[1] MARC VOGEL,[2] DNYANESHWAR B. GOPHANE,[3] JULIA E. WEIGAND,[2] BEATRIX SUESS,[2] SNORRI TH. SIGURDSSON,[3] and THOMAS F. PRISNER[1]

[1]Institute of Physical and Theoretical Chemistry and Center of Biomolecular Magnetic Resonance, Goethe University Frankfurt, 60438 Frankfurt am Main, Germany

[2]Department of Biology, Technical University of Darmstadt, 64287 Darmstadt, Germany

[3]Department of Chemistry, Science Institute, University of Iceland, 101 Reykjavik, Iceland

ABSTRACT

The tetracycline-binding RNA aptamer (TC-aptamer) is a synthetic riboswitch that binds the antibiotic tetracycline (TC) with exceptionally high affinity. Although a crystal structure exists of the TC-bound state, little is known about the conformational dynamics and changes upon ligand binding. In this study, pulsed electron paramagnetic resonance techniques for measuring distances (PELDOR) in combination with rigid nitroxide spin labels (Çm spin label) were used to investigate the conformational flexibility of the TC-aptamer in the presence and absence of TC at different Mg^{2+} concentrations. TC was found to be the essential factor for stabilizing the tertiary structure at intermediate Mg^{2+} concentrations. At higher Mg^{2+} concentrations, Mg^{2+} alone is sufficient to stabilize the tertiary structure. In addition, the orientation of the two spin-labeled RNA helices with respect to each other was analyzed with orientation-selective PELDOR and compared to the crystal structure. These results demonstrate for the first time the unique value of the Çm spin label in combination with PELDOR to provide information about conformational flexibilities and orientations of secondary structure elements of biologically relevant RNAs.

Keywords: tetracycline aptamer; conformational flexibility; divalent metal ions; PELDOR; DEER; synthetic riboswitches

INTRODUCTION

Over past years, the role of RNAs in life sciences has changed from a pure information carrier in protein biosynthesis to a more active component in gene regulation. One of the new roles for RNAs are riboswitches, which are typically found in the untranslated regions of bacterial mRNA and bind specific small molecules with high affinity. Binding of the ligand leads to a conformational change of the aptamer domain, which in turn alters gene regulation. Based on this concept, artificially engineered riboswitches have attracted attention, with the ultimate goal of using engineered riboswitches in gene therapy (Breaker 2012; Groher and Suess 2014; Hallberg et al. 2017).

A promising synthetic riboswitch is the approximately 60 nucleotide (nt) long tetracycline aptamer (TC-aptamer), discovered by SELEX in the Schroeder laboratory (Berens et al. 2001), that binds the antibiotic TC (Fig. 1A). Besides the nontoxicity and good cell permeability of TC (Chopra and Roberts 2001), several other aspects make the TC-aptamer widely used as a synthetic riboswitch. Firstly, the TC-aptamer exhibits a K_d value in the sub-nanomolar range (K_d = 800 pM), which is one of the highest affinities of an aptamer toward its ligand (Müller et al. 2006). Secondly, the TC-aptamer is one of the few aptamers that is known to function as a riboswitch in vivo, where it can control translation and splicing (Weigand and Suess 2007; Kötter et al. 2009; Vogel et al. 2018). Although several small molecule binding aptamers have been selected, only a few aptamers show riboswitch activity in vivo, namely the tetracycline, the theophylline, the neomycin and the biotin aptamer (Berens et al. 2015).

Therefore, a series of experimental studies have been performed in order to investigate which structural motifs are responsible for the unique properties of the TC-aptamer. Hanson and coworkers showed by using chemical probing experiments, in combination with fluorescence measurements, that loop 3 (*L3*, cyan in Fig. 1B,

Corresponding author: prisner@chemie.uni-frankfurt.de

Article is online at http://www.rnajournal.org/cgi/doi/10.1261/rna.068684.118.

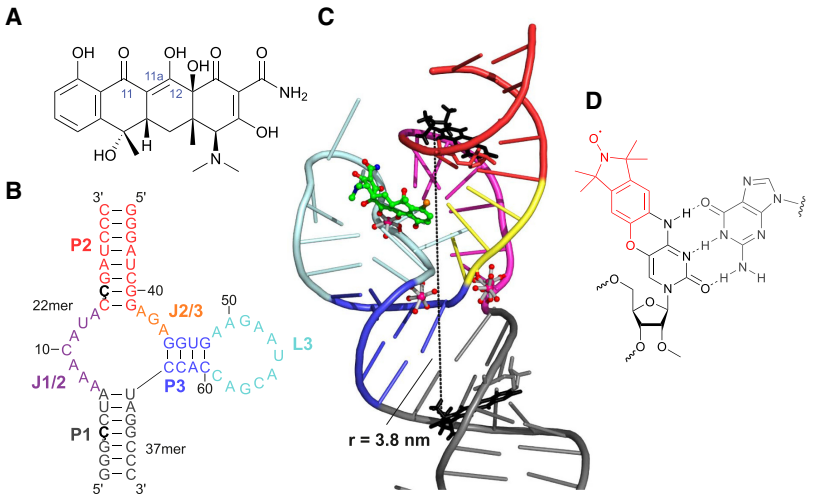

FIGURE 1. (*A*) Chemical structure of the antibiotic TC. Metal ligation typically occurs via O11 and O12. (*B*) Secondary structure of the TC-aptamer as used for Mg^{2+} titration experiments. Two Çm nucleosides are shown in black. (*C*) Cartoon representation of a TC-binding RNA aptamer based on the crystal structure by Xiao et al. (2008). Selected Mg^{2+}-ions are shown in magenta. TC is shown in green. Two rigid nitroxide spin labels (Çm) were attached to the crystal structure (shown in black). The expected distance between the two unpaired electron spins is 3.8 nm. (*D*) Chemical structure of Çm. Two covalent bonds between the nitroxide moiety (red) and cytidine significantly reduce the internal flexibility of Çm.

C) is crucial for binding of TC (Hanson et al. 2005), which was later confirmed by the crystal structure of the TC-aptamer bound to its cognate ligand (Xiao et al. 2008). The tertiary structure was found to be fairly complex, resembling an "h-shaped" structure that is reminiscent of larger, natural occurring riboswitches and rather unusual for other aptamers of comparable size (McCown et al. 2017). The crystal structure also revealed that TC binds as a Mg^{2+}-ion chelate to the aptamer (Fig. 1C). The TC chelate complex is further stabilized by a series of noncovalent interactions with different nucleotides in the binding pocket. In addition, more Mg^{2+} ions were found to bind near junctions *J1/2* and *J2/3* of the aptamer. Although a crystal structure yields a highly resolved three-dimensional picture, care has to be taken of interpreting structural motifs and their function solely based on crystal structure data (Nelson and Uhlenbeck 2006). It cannot be deduced from the crystal structure on how the tertiary structure looks in the absence of TC or how the Mg^{2+} concentration affects RNA folding and ligand binding. In addition, crystal-packing effects can distort the physiological conformation.

To answer these questions, Wunnicke and coworkers performed EPR (electron paramagnetic resonance) experiments on a nitroxide-labeled TC-aptamer in the absence and presence of TC (Wunnicke et al. 2011). They proposed a tertiary structure in the absence of TC in which mainly the junction *J1/2* between the stems *P1* and *P2* gets displaced. Förster and coworkers used time-resolved fluorescence measurements of the ligand TC to investigate the folding kinetics of the wild-type aptamer and three mutants (Förster et al. 2012). It was found that the ligand binds to the aptamer in a two-step process. In a first reversible process, the ligand is recognized by the RNA. In a second irreversible reaction, the aptamer forms its final tertiary structure. Out of the three mutants, mutant A9G had the strongest impact on the folding kinetics. Here, the kinetics were slowed down by several orders of magnitude. In a follow-up study, Reuss and coworkers examined the influence of Mg^{2+} concentration on the folding kinetics and thermodynamics of the aptamer by using isothermal titration calorimetry (ITC), circular dichroism (CD) spectroscopy, fluorescence spectroscopy, and melting studies. Among others, it was concluded that at high Mg^{2+} concentrations (>1.5 mM), the aptamer adopts its near-final tertiary structure, even in the absence of TC (Reuss et al. 2014).

In the present study, we used pulsed electron–electron double resonance spectroscopy (PELDOR, also called DEER) (Milov et al. 1981; Pannier et al. 2000) to measure intramolecular distances and thereby conformational flexibility of a frozen conformational ensemble of a doubly nitroxide-labeled TC-aptamer at different Mg^{2+} concentrations in the presence and absence of TC. In PELDOR, the integrated echo intensity of a refocused Hahn echo (RHE) is monitored as a function of the incremented time t before the pump pulse with the microwave frequency ν_B (Fig. 2A). As a result, the recorded PELDOR time traces oscillate with the dipolar coupling frequency ω_{dd}, which is inversely proportional to r^3. Tikhonov regularization of background-corrected PELDOR time traces (Fig. 2B, left) then yields a probability function $P(r)$ for the distance distribution (Fig. 2B, right). Another important parameter besides the distance distribution $P(r)$ is the modulation depth Δ. For a pure 2-spin system (as shown schematically in Fig. 2A) and experimental parameters of our Q-band experiments (see "Q-band PELDOR" section), Δ cannot exceed a value of 0.25 (or 25%).

As nitroxide spin probes we utilize the rigid and nonperturbing Çm spin label (Fig. 1D; Höbartner et al. 2012). In the study by Höbartner et al. (2012), thermodynamic melting experiments and CD spectroscopy on small RNA helices showed that insertion of the Çm spin label yields only small, negligible differences in comparison to an unmodified RNA. Rigid nitroxide spin labels, such as Çm, offer several advantages over flexible nitroxide spin labels. Due to the negligible internal freedom of motion of rigid spin

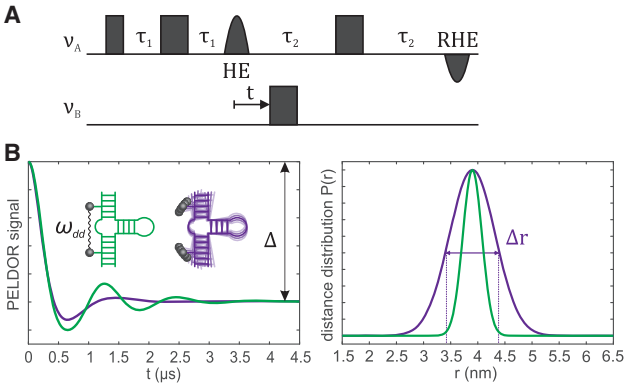

FIGURE 2. (*A*) Pulse sequence of a four-pulse PELDOR experiment (Pannier et al. 2000). The integrated echo intensity of the refocused Hahn echo (RHE) at $2\tau_1 + 2\tau_2$ is monitored as a function of the time *t* between the initial Hahn echo (HE) and the pump pulse with frequency ν_B. (*B*) Simulated PELDOR time traces (*left*) for a Gaussian distribution of distances centered at 3.9 nm (*right*). Two different distribution widths Δr (FWHM) of 0.4 nm (green) and 0.95 nm (purple) were simulated. Larger Δr values correspond to a higher conformational flexibility of the nitroxide-labeled helices, which causes a stronger dampening of the oscillations in the time domain. The PELDOR traces oscillate with the dipolar coupling frequency ω_{dd}, which is inversely proportional to r^3.

labels, the distance distributions *P*(*r*) tend to exhibit a small full width at half maximum (FWHM, Δr). Therefore, the distances and their distribution can be directly related to the structure and conformational flexibility of the nucleic acid itself. Thus, a system with high conformational flexibility would yield rather strongly dampened oscillations in the time domain and a broad probability distribution *P*(*r*) in the distance domain (purple data in Fig. 2B). Vice versa, a low degree of conformational flexibility would yield pronounced oscillations with a narrow probability distribution *P*(*r*) (green data in Fig. 2B).

More importantly, rigid spin labels can be used to study the relative orientation of two helices with respect to each other, a phenomenon that is typically referred to as orientation selection. Orientation selection of the rigid Çm spin label was first reported by Tkach and coworkers on an RNA model duplex (Tkach et al. 2013). Grytz and coworkers used the rigid Ç spin label, a derivative of Çm for DNA molecules, to determine helix orientations of a cocaine-binding DNA aptamer and a flexible DNA-motif (Grytz et al. 2016, 2017). Long-distance restraints of PELDOR measurements were combined with short-distance nuclear magnetic resonance (NMR) restraints to propose a global three-dimensional structure of a flexible DNA-motif (Grytz et al. 2017).

Thus, PELDOR in combination with rigid spin labels allows investigating the conformational flexibility of selected secondary structure elements in a parameter-free approach. The results of this study complement the aforementioned recent findings by Förster et al. (2012) and Reuss et al. (2014), where the conformational dynamics of a TC-aptamer were studied by performing melting, ITC, and CD studies of the whole aptamer itself and by looking at the fluorescence of the ligand. Whereas these latter two aforementioned studies examine kinetic and thermodynamic properties, such as free energies and rate constants, the present study quantitatively determines structural data such as distances and angular information and relates it to the conformational flexibility of the aptamer.

RESULTS AND DISCUSSION

In order to facilitate spin-labeling of the aptamer, the construct was separated into two components. As helices *P1* and *P2* are part of the scaffold and loop *L2* is not important for either binding of the ligand or folding of the aptamer, loop L2 was removed (Hanson et al. 2003; Suess et al. 2003), thus separating the TC-aptamer. The complete TC-aptamer (Fig. 1A) was then restored by hybridization of the two single strands. Entire hybridization and unaltered binding affinity toward TC was verified with native PAGE (Supplemental Fig. S2) and ITC measurements (Supplemental Fig. S3). The labeling positions were chosen as close to the binding pocket as possible, but without directly influencing it to ensure correct ligand binding. In silico simulations based on the crystal structure did not indicate any sterical clashes for the labeling position shown in Figure 1B.

The "Results" section is structured as follows: At first, PELDOR Mg^{2+}-titration studies at Q-band frequencies (≈34 GHz) in the absence and presence of TC are presented to investigate the conformational flexibility of the TC-aptamer. Q-band is the preferred microwave frequency for the titration studies, as here the influence of orientation selection is negligibly small, due to similar sizes of the g-tensor and hyperfine-tensor anisotropies. In this case, the distance distribution *P*(*r*) is free of any artificial peaks due to orientation selection. In a second step, orientation-selective PELDOR measurements at X-band frequencies (≈9.4 GHz) are presented to determine the relative orientation of the two Çm-labeled helices. At 9.4 GHz, the anisotropy of the hyperfine coupling of the ^{14}N-nucleus dominates the spectral shape, whereas the anisotropy of the electron Zeeman interaction is negligible (Supplemental Fig. S4). Therefore, different orientations can be excited by using different offsets $\Delta\nu$ ($\Delta\nu = \nu_A - \nu_B$). By combining PELDOR measurements at Q-band and X-band, distance information obtained at Q-band can be verified and directly related to the orientation of the crystal structure.

Structural changes of the TC-aptamer upon adding TC and/or Mg^{2+}

The conformational flexibility of the TC-aptamer was investigated with PELDOR spectroscopy as a function of different Mg^{2+} concentrations in the presence or absence of TC. Mg^{2+} concentrations of 0.22 mM, 0.45 mM, 1.2 mM, and 3.0 mM were chosen to mimic physiological Mg^{2+}

concentrations (Saris et al. 2000). For rigid spin labels, the probability function $P(r)$ of Q-band PELDOR data contains (i) information about the intramolecular distance of the two spin labels and (ii) information about the conformational flexibility of the macromolecule (width Δr of a distance peak).

Figure 3 shows PELDOR time traces and distance distributions of samples containing the TC-aptamer in the presence (Fig. 3A) or absence (Fig. 3B) of TC at different Mg^{2+} concentrations. For the "maximum" Mg^{2+} concentration of 3.0 mM (green) in the presence of TC, clear PELDOR oscillations, which correspond to a distance of 3.9 nm, are visible. This value is in very good agreement with the distance obtained from the crystal structure ($r_{X\text{-}ray} = 3.8$ nm). The main distance peak is characterized by a very narrow width of $\Delta r = 0.4$ nm. Thus, the tertiary structure of the TC-aptamer seems to have a low conformational flexibility at high Mg^{2+} concentrations in the presence of TC. For "intermediate" Mg^{2+} concentrations of 0.22 mM (violet), 0.45 mM (yellow), and 1.2 mM (cyan) the width of the main distance peak at 3.9 nm changes only slightly. Here, Δr increases from 0.4 nm for 1.2 mM Mg^{2+}, over 0.5 nm for 0.45 mM Mg^{2+} to 0.6 nm for 0.2 mM Mg^{2+} (Fig. 4).

In the absence of Mg^{2+} (red), the distance distribution is dominated by a very broad component at shorter distances. Due to the broad distribution width, it is impossible to give a quantitative interpretation. However, it is likely that the TC-aptamer adopts a variety of unfolded meta-stable structures in the absence of Mg^{2+}, hence yielding many distances and therefore a broad distance distribution. In general, shorter distances become more probable with decreasing Mg^{2+} concentrations (Fig. 3A, right). Therefore, it appears that an Mg^{2+}-dependent equilibrium exists between the well-defined folded tertiary structure and an ensemble of unfolded meta-stable conformations.

Figure 3B shows Q-band PELDOR time traces and distance distributions of samples containing the TC-aptamer at different Mg^{2+} concentrations in the absence of TC. PELDOR and distance data at 3 mM Mg^{2+} in the absence of TC (Fig. 3B, green) are essentially identical to the PELDOR trace and distance distribution shown in the presence of TC (Fig. 3A, green). Therefore, at 3 mM Mg^{2+}, TC is a negligible factor in formation and stabilization of the tertiary structure of the TC-aptamer.

This picture, however, changes when analyzing and comparing PELDOR data at "intermediate" Mg^{2+} concentrations (violet, yellow, and cyan data in Fig. 3B). Here, the widths of the main distance peaks are always broader than the equivalent distance peaks shown in Figure 3A (with TC). This becomes also apparent by looking at Figure 4, where the Δr values of the distance distributions of Figure 3 are plotted as a function of the Mg^{2+} concentration. For example, the yellow distance peak in Figure 3B (0.5 mM Mg^{2+}, without TC) is broader than the yellow distance peak in Figure 3A (0.5 mM Mg^{2+}, with TC). Both peaks, however, share an identical mean distance of 3.9 nm. In the absence of TC, Δr increases more drastically than in the presence of TC from 0.6 nm for 1.2 mM Mg^{2+}, over 0.8 nm for 0.45 mM Mg^{2+} to 1.5 nm for 0.2 mM Mg^{2+} (Fig. 4). This shows, that at "intermediate" Mg^{2+} concentrations, TC is essential for stabilizing the folded tertiary structure of the aptamer. In other words, in the presence of TC, intermediate concentrations of Mg^{2+} are already sufficient to significantly reduce the conformational flexibility of the folded tertiary structure of the aptamer. The PELDOR time trace and distance data without TC and any Mg^{2+} (red in Fig. 3B) are nearly identical to the time trace and distance data without any Mg^{2+} but in the presence of TC (red in Fig. 3A). This finding is not surprising, as it is

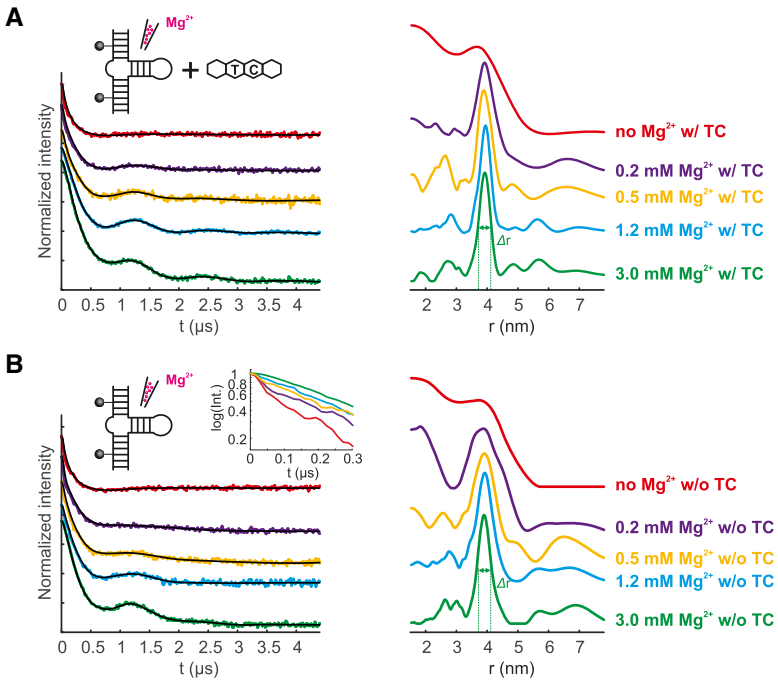

FIGURE 3. (*A*) Background-corrected Q-band PELDOR time traces and distance distributions $P(r)$ obtained by Tikhonov regularization of 150 µM TC-aptamer and 165 µM TC with varying Mg^{2+} concentrations. (*B*) Background-corrected Q-band PELDOR time traces and distance distributions $P(r)$ obtained by Tikhonov regularization of 150 µM TC-aptamer with varying Mg^{2+} concentrations. The *inset* on the *left* shows a half-logarithmic plot of the first 300 ns of background-corrected PELDOR time traces, which illustrates an increased probability for smaller distances with lower Mg^{2+} concentrations. The fits of the Tikhonov regularization are shown in black.

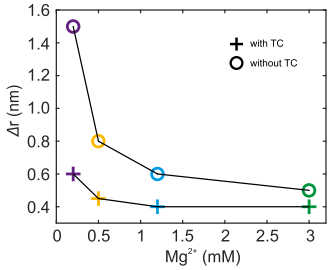

FIGURE 4. Width Δr (full width at half maximum) of the main distance peaks at 3.9 nm of the distance distributions shown in Figure 3 as a function of Mg^{2+} concentration. The color code is identical to Figure 3. Plus signs label samples in the presence of TC, whereas circles label samples in the absence of TC. The width Δr of samples without TC increases more strongly with decreasing Mg^{2+} concentration than for samples with TC. Samples containing no Mg^{2+} are not included in this plot, as here no reliable Δr values could be extracted.

generally known that Mg^{2+} is needed for folding of the TC-aptamer. For a direct comparison of data sets with the same Mg^{2+} concentration with and without TC, the reader is referred to Supplemental Figure S6.

The trend of increasing Δr values for decreasing Mg^{2+} concentrations is also consistent with an increased dampening of the PELDOR oscillations for decreasing Mg^{2+} concentrations. A stronger dampening of the oscillations in the time domain causes a broader distribution width in the distance domain (Fig. 2B). Consequently, a stronger dampening reflects an increased conformational flexibility of the RNA helices. For example, the yellow PELDOR time trace in Figure 3B (0.45 mM Mg^{2+}, without TC) exhibits a stronger dampening than the yellow PELDOR time trace in Figure 3A (0.45 mM Mg^{2+}, with TC). Therefore, the trend of Δr values is already clearly visible in the background-corrected PELDOR time traces.

Just as in Figure 3A, distance data in Figure 3B also show an increased probability for shorter distances with decreasing Mg^{2+} concentration. This behavior becomes more apparent when looking at the inset of Figure 3B, which shows a half-logarithmic plot of the first 300 ns of background-corrected and modulation-depth scaled PELDOR data. Here, a steeper slope corresponds to an increased probability of shorter distances in the distance domain. Due to the rather broad and unspecific profile of the distance distributions in the region from 1.8 to 3.0 nm, we did not attempt to compare these regions between Figure 3A (with TC) and Figure 3B (without TC) in a quantitative manner. It seems, however, that in the absence of TC, the aforementioned equilibrium is more shifted toward the side of metastable conformers.

In theory, intramolecular self-hybridization of the spin-labeled monomer (22-mer in Fig. 1B) could also yield small distances similar to those that were observed in Figure 3A,B. However, the helices were designed in such a way that the heterodimer is thermodynamically significantly more favorable than the monomer. The predicted free energy of the heterodimer was calculated to $\Delta G_{hetero} = -30.0$ kcal/mol, whereas the predicted free energy of the spin-labeled monomer was calculated to $\Delta G_{mono} = -1.2$ kcal/mol (Gruber et al. 2008). In addition, no band corresponding to a self-hybridized 22-mer was observed on a control gel (Supplemental Fig. S2). We therefore exclude the possibility of a self-hybridized monomer.

Helical stacking between TC-aptamers

The PELDOR time traces at 3 mM Mg^{2+} (Fig. 3A,B, green) seem to contain longer distances ($r > 5$ nm), as here the minimum of the first oscillation is not the overall minimum. In addition, the time traces with 3 mM Mg^{2+} exhibit a fairly large modulation depth Δ ($\Delta = 0.4$ for a sample with 3 mM Mg^{2+} and no TC). Multispin systems, where the number of intramolecular spins N is >2, are known to increase the modulation depth Δ (von Hagens et al. 2013).

Large distances and large modulation depths are indicative of RNA stacking, a phenomenon in which RNA helices stack on top of each other (Piton et al. 2007; Krstić et al. 2011). In our case (rather broad and undefined), distances at 3 nm and from 5 nm to 7 nm (asterisks in Supplemental Fig. S8D) could be explained by a very simplified model, in which two spin-labeled aptamers were stacked on top of each other (Supplemental Fig. S7). In addition, the modulation depth Δ exhibits a clear dependence on the Mg^{2+} concentration (Supplemental Fig. S8E). This correlation is reasonable, as negatively charged divalent metal ions are likely to act as bridging ions between two negatively charged RNA duplex ends. Thus, a higher Mg^{2+} concentration facilitates stacking, which manifests itself in an increased modulation depth Δ.

To test whether our results were due to helical RNA stacking, TC-aptamers with different single-nucleotide overhangs were prepared (Supplemental Fig. S8A). Q-band PELDOR revealed that construct II was essentially free of any stacking artifacts (no additional distances and no increased modulation depth), indicating that a pyrimidine-nucleotide overhang (cytidine, construct II) is more efficient in preventing end-to-end stacking than a purine-nucleotide overhang (guanine, construct III). This is reasonable, as a computational study recently showed that G-G-nucleobase-dimers are expected to be more prone to π–π-stacking than C-C-nucleobase-dimers (Mignon et al. 2005). Similar findings were recently reported by Weinrich and coworkers on a TAR-RNA system (Weinrich et al. 2018).

Orientation-selective PELDOR at X-band yields data in agreement with the X-ray crystal structure

Construct II (Supplemental Fig. S8A) was subsequently used to perform orientation-selective PELDOR

measurements at X-band frequencies with the goal of extracting the relative orientation of the two spin labeled RNA helices. Orientation-selective PELDOR with construct I and construct III would be much more challenging, as stacking artifacts can severely hamper data analysis of orientation-selective PELDOR experiments. The orientation-selective measurements were performed in the presence of 3 mM Mg^{2+} and TC.

The orientation of two nitroxide spin labels with respect to each other can be described by six parameters, namely the distance vector *r* (chosen to be parallel to the *z*-axis of the dipolar coordinate system), two Euler angles β_1 and γ_1 of nitroxide spin label 1 (because of symmetry the *x*-axis can be freely chosen, therefore the first Euler angle is set arbitrarily to $\alpha_1 = 0$) and the three Euler angles α_2, β_2, and γ_2 of nitroxide spin label 2. Euler angles describe the relative orientation of the principal axis system of a nitroxide spin label to the dipolar coordinate system, whose *z*-axis coincides with the distance vector *r*. Recent publications have focused on a detailed theoretical explanation and simulation of orientation-selective PELDOR data (Larsen and Singel 1993; Abé et al. 2012; Marko and Prisner 2013; Prisner et al. 2015). Therefore, only a brief summary about orientation-selective PELDOR at X-band frequencies is given here.

At X-band frequencies (9.4 GHz) the anisotropy of the ^{14}N-hyperfine interaction of nitroxide radicals dominates the spectral shape of the echo-detected field-swept spectrum. This becomes apparent by comparing the simulated field-swept spectra with its nitrogen hyperfine components at X-band and Q-band frequencies, respectively (Supplemental Fig. S4A,B). For X-band frequencies, different spin orientations can be excited by the detection pulses when using different pump/probe $\Delta\nu$ offsets, which typically range from 40 MHz to 90 MHz. The excitation of different orientations manifests itself in different oscillation patterns and modulation depths for different offsets $\Delta\nu$. By fitting orientation-selective X-band PELDOR data (Marko and Prisner 2013), mainly the orientation of the *z*-components z_1 and z_2 of the two hyperfine tensors with respect to the dipolar vector *r*, and therefore the bend angle ϕ between two RNA helices can be deduced (Fig. 5B). For more information, the reader is referred to Section S9 in the Supplemental Material.

Figure 5A shows background-corrected X-band PELDOR data with different pump/probe offsets. As expected, orientation selection manifests itself in different oscillation patterns for different offsets (the oscillation for $\Delta\nu = 90$ MHz is longer than the oscillation for $\Delta\nu = 40$ MHz). In addition, the modulation depth increases constantly from $\Delta_{40\ MHz} = 0.36$ to $\Delta_{90\ MHz} = 0.53$. Orientation selection manifests itself also in distortions of the Pake patterns obtained by Fourier transformation of the PELDOR time traces shown in Figure 5A (Supplemental Fig. S10).

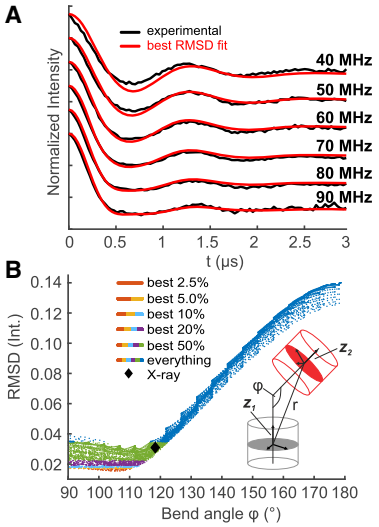

FIGURE 5. (*A*) Background-corrected X-band PELDOR time traces of 150 µM TC-aptamer (construct II, see Supplemental Fig. S8), 165 µM TC and 3 mM Mg^{2+} with different pump/probe offsets. Simulated PELDOR time traces with Euler angles that yielded the best RMSD are shown for comparison in red [$\alpha_1 = 0$ (0), $\beta_1 = 0.94$ (0.42), $\gamma_1 = -1.82$ (−1.82), $\alpha_2 = -0.88$ (−0.88), $\beta_2 = 2.63$ (2.36), $\gamma_2 = 2.06$ (2.06), given in radians, values in brackets correspond to the crystal structure]. (*B*) RMSD of PELDOR simulations with different sets of Euler angles as a function of the bend angle ϕ. β_1, α_2, and β_2 were varied around the Euler angles of the crystal structure in 5° increments (10 steps ± the start value = 21^3 simulations). The bend angle ϕ between the two RNA helices (red and gray helices in Fig. 1A,C) was calculated out of the angles β_1, α_2, and β_2. The bend angle of the crystal structure with its RMSD is shown as a black diamond.

In a next step, the Euler angles of spin labels that were attached to the X-ray crystal structure, were simulated, and compared to experimental data (Supplemental Fig. S11B). Although the oscillation pattern for smaller offsets could be reproduced by the simulation, a clear discrepancy is visible for larger offsets (80 MHz and 90 MHz). Therefore, the Euler angles β_1, α_2, and β_2 were varied in ±5° increment steps around the values obtained from the X-ray structure, 10 steps in each direction, thus yielding 21^3 different orientations that were simulated. The angles α_1, γ_1, γ_2 and the distance vector *r* were kept constant, because they are not sensitive to X-band PELDOR data (Abé et al. 2012; Marko and Prisner 2013). The quality of each simulation was evaluated by calculating the root mean square deviation (RMSD) over the whole length of the time traces. Simulations with Euler angles that yielded the best RMSD are shown in Figure 5A as red time traces. It should be mentioned that the ambiguities arising from the insensitivity of PELDOR to the sign of the z_1 and z_2 vectors do not apply in this approach (Abé et al. 2012). This is because for the present study prior knowledge about the molecular model is available by the crystal structure. Furthermore, the indistinguishability of the two spin labels is of no concern for data presented

within this study. This is based on the fact that the bend angle ϕ describes the relative orientation of the two spin labels and not the absolute position of each spin label (Abé et al. 2012).

For a better visualization, each orientation of the two spin labels, as defined by the three Euler angles β_1, α_2, and β_2, was transformed into the bend angle ϕ (for an explanation of the bend angle ϕ, see the inset of Fig. 5B or Section S9 of the Supplemental Material). The RMSD was then plotted as a function of the bend angle ϕ (Fig. 5B) and compared to the angle ϕ that was extracted from spin labels attached to the crystal structure (black diamond in Fig. 5B). The simulations exhibit a minimum bend angle at $\phi_{fit} = 106°$, which was in a reasonable agreement with the calculated angle of $\phi_{X\text{-}ray} = 118°$ for the crystal structure. Thus, the analysis of orientation-selective PELDOR data confirms that the structure obtained in frozen solution is in agreement with the structure obtained from X-ray data. The small deviation could indicate minor structural rearrangements due to crystal packing effects.

More simulated PELDOR time traces, including Euler angles that yielded the worst RMSD (within the given 5° variations) are presented in the supporting information (Supplemental Fig. S11). We also applied an iterative fitting algorithm, that was recently developed in our group (Marko and Prisner 2013), to the X-band PELDOR data. In this approach, the data were fitted over *n* iterative steps. In each step, the best-fitting simulated time trace for a conformer from a simulated library off all possible conformers was chosen. The collection of the best-fitting conformers of size *n* shows a very narrow distribution of its bend angles (Supplemental Fig. S12, middle row). In addition, the mean bend angle of this iterative fitting approach agrees perfectly with the best bend angle of Figure 5B, thus emphasizing the uniqueness of the simulation results presented in this study. The Δr values of the conformers shown in Figure 5A and Supplemental Figure S12 are also in very good agreement with experimental Δr values obtained from Q-band data (Supplemental Fig. S13).

We also recorded orientation-selective X-band PELDOR data at "intermediate" Mg^{2+} concentrations of 0.45 mM (Supplemental Figs. S14–S16). Simulations did not reveal significantly different best Euler and bend angles than for 3.0 mM Mg^{2+} and in the presence of TC. The results of Mg^{2+}-titration studies ("Structural changes of the TC-aptamer upon adding TC and/or Mg^{2+}" section) were, however, confirmed: Both orientation-selective PELDOR data for 0.45 mM Mg^{2+} in Supplemental Figure S15A,B exhibit a steeper slope at the beginning than orientation-selective PELDOR data with 3.0 mM Mg^{2+}. A steeper slope at the beginning corresponds to a higher probability for smaller distances. Just as with the Q-band Mg^{2+} titration studies, orientation-selective X-band PELDOR data with 0.45 mM Mg^{2+} in the absence of TC are characterized by stronger dampening of the oscillations than the orientation-selective PELDOR data with 0.45 mM Mg^{2+} in the presence of TC, which is consistent with a larger Δr value in the distance domain (Supplemental Fig. S16).

Conclusion

Besides yielding accurate intramolecular distances, the PELDOR time traces of the TC aptamer containing a pair of rigid spin labels provided more information about the dynamics and conformational flexibility of the aptamer.

Firstly, the width Δr of the main distance peak is a sensitive indicator for the intramolecular flexibility of the tertiary structure. More specifically, it was shown that the tertiary structure of the TC-aptamer needs TC at "intermediate" Mg^{2+} concentrations (0.22–1.2 mM) to form a stable tertiary structure. At a certain point (≥3 mM), Mg^{2+} alone is sufficient to stabilize the tertiary structure of TC. These results are in perfect agreement with recent findings by the Wachtveitl group on the TC-aptamer using fluorescence, ITC, CD, and melting studies (Reuss et al. 2014). Whereas the above-mentioned techniques look at the aptamer as a whole (melting point, ITC, or CD studies) or just at the ligand itself (fluorescence), PELDOR sheds light on selected secondary structure elements of RNA molecules. In the study by Reuss et al. (2014), a model was proposed in which the structure of the aptamer is in a preformed condition at intermediate Mg^{2+} concentrations and in the absence of TC. With the addition of TC, the final tertiary structure is formed out of the preformed conformation. The results of this study are in perfect agreement with the model by Reuss and coworkers – PELDOR is able to sample the preformed state by means of a broader distance distribution width at intermediate Mg^{2+} concentrations in the absence of TC (Fig. 3B).

Secondly, the relative orientation of the two helices *P1* and *P2* (Fig. 1A,B) could be investigated using orientation-selective PELDOR measurements. The relative orientation of the two helices agrees well with the X-ray crystal structure of the TC-aptamer in the TC-bound state. Given a good experimental signal-to-noise ratio, orientation-selective PELDOR in combination with rigid spin labels is therefore a sensitive method to study orientations of secondary structure elements of RNA molecules. This is of particular interest, as PELDOR (and pulsed dipolar EPR spectroscopy in general) is not restricted to size limitations as in NMR. In the present study, X-band PELDOR was used to determine an ≈10° difference of the bend angle ϕ between the two double-stranded helices *P1* and *P2* compared to the X-ray structure. PELDOR time traces simulated with the bend angle of the crystal structure ($\phi_{X\text{-}ray}$) revealed an experimentally significant different oscillation pattern than the experimental PELDOR time traces and exhibited a significant larger RMSD compared to simulations with the 10°-changed bend angle ϕ_{fit}. Two different fitting approaches (starting from the X-ray structure and ab initio iterative fitting of the PELDOR time traces) essentially

yielded identical results (bend angles), thus emphasizing the correctness of our simulations.

This study clearly illustrates the benefits of using rigid spin labels in combination with PELDOR measurements to study structural dynamics of nucleic acids. To our knowledge, this is the first time that the unique properties of the Çm spin label have been used to answer relevant questions about biologically active RNA systems. It should be noted that these results could not have been obtained with flexible spin labels, simply because the rotational freedom around the tether eliminates all orientation selection and gives rise to a broad signal in the distance distribution $P(r)$ that renders a detailed interpretation of the distance distribution width Δr impossible. The rotational freedom around the linker would also inhibit determination of additional angular restraints.

MATERIALS AND METHODS

RNA synthesis and purification

In order to facilitate synthesis of a spin-labeled construct, the aptamer was composed of two parts, a 5′ 22-mer and a 3′ 37-mer. After annealing, a complete TC-aptamer (Fig. 1B) can be restored.

The 22-mer of the construct shown in Figure 1B was synthesized via solid phase synthesis as described previously (Tkach et al. 2013) and analyzed by MALDI-TOF analysis (Supplemental Fig. S1). For more information on the synthesis of the 22-mer, the reader is referred to Section 1 of the Supplemental Material.

The 37-mer of the construct shown in Figure 1B was in vitro transcribed by enzymatic synthesis using a *Sma*I linearized plasmid as template. The plasmid codes for the T7 promoter followed by the aptamer sequence (the full plasmid sequence is available upon request). In vitro transcription was performed at 37°C overnight in a total volume of 10 mL containing 20 mM magnesium acetate, 0.2 M Tris-HCl pH 8.0, 20 mM DTT, 2 mM spermidine, 0.2 mg/mL linearized plasmid, 4 mM of each NTP, and 7.5 mg/mL of T7 polymerase (made in-house). After transcription, precipitated pyrophosphate was pelleted by centrifugation and 10% (v/v) EDTA (0.5 mM, pH 8.0) was added to the supernatant. Ethanol precipitation was performed and the RNA was purified by a denaturing polyacrylamide gel electrophoresis (10% PAA, 8 M urea). The RNA was detected via ultraviolet (UV) shadowing, cut out, and eluted from the gel in 0.3 M sodium acetate pH 6.5 at 4°C overnight. To remove the remaining gel slices, the supernatant was filtered using a 0.45 mm filter (Sarstedt) and again the RNA was precipitated using ethanol. Finally, the RNA was dissolved in double-distilled water and stored at −20°C.

The "right" RNA strands of constructs II and III (39-mer and mod 37-mer, see Supplemental Fig. S8A) were prepared as described in the previous paragraph. After purification, the "right" RNA strands of construct I, II, and III (Supplemental Fig. S8A) were hybridized with the "left" strand (22-mer) by mixing an equimolar amount of each RNA strand in water. The reaction mix was incubated at 95°C for 2 min and afterward temperature was reduced to 25°C by 1°C per minute. The hybridized RNA was stored at −20°C. Complete hybridization of the aptamer was checked by native PAGE (Supplemental Fig. S2).

ITC measurements

K_d measurements were determined by ITC experiments (Vogel and Suess 2016). ITC measurements of an unlabeled hybrid TC-aptamer were compared to ITC measurements of the Çm-labeled hybrid TC-aptamer. Both hybrids, the unlabeled construct (K_d = 6.5 nM) and the labeled construct (K_d = 7.0 nM), had identical binding constants as the full-length aptamer (Reuss et al. 2014), ensuring correct ligand binding. Thus, our hybrid aptamer faithfully recapitulates ligand binding and is a suitable model for structural analyses. For more details on ITC measurements, the reader is referred to Section 3 of the Supplemental Material and Supplemental Figure S3.

Sample preparation for EPR measurements

Aliquots of the frozen RNA solution were lyophilized and dissolved in a solution of D_2O containing 20 mM triethanolamine, 100 mM sodium chloride, and varying amounts of magnesium chloride (from 0 mM to 3 mM) at pH = 7.0. Twenty percent of the solution was deuterated ethylene glycol (v/v), used as a glassing agent. For X-band PELDOR samples, only the glassing agent was deuterated. The final RNA concentration was 150 µM. For PELDOR measurements in the presence of TC, the buffer solution also contained 165 µM of TC. All chemicals were certified RNase-free. RNA samples were transferred into 1.6 mm OD Suprasil tubes (10 µL) or 2.8 mm OD quartz tubes (20 µL) for Q-band and X-band PELDOR measurements, respectively. Samples were shock-frozen in liquid nitrogen *prior* to being inserted into the resonator.

X-band PELDOR

PELDOR measurements at X-band frequencies (≈9.4 GHz) were performed on a homebuilt X-band spectrometer equipped with a split-ring ER 4118X MS3 probehead. More details regarding the spectrometer design will be published elsewhere. A 1 kW traveling-wave tube by Applied Systems Engineering was used for microwave amplification. Temperature was kept at 50 K using a continuous-flow helium cryostat (CF935) and an ITC 502 temperature control unit, both from Oxford Instruments. The pump pulse was chosen to coincide with the maximum of the echo-detected field-swept spectrum. Detection was performed at frequency offsets between pump and probe pulses of $\Delta\nu$ = 40, 50, 60, 70, 80, and 90 MHz (Supplemental Fig. S4A contains a simulated echo-detected field-swept spectrum with visualized pump/probe positions and pulse excitation profiles). Detection pulses had a length of 32 ns, pump pulses were optimized for a length of 12 ns. Tau values of τ_1 = 430 ns and τ_2 = 3500 ns were used. The shot repetition time was set to 4 µs. A tau averaging cycle of 8 × 56 ns was used in order to suppress deuterium modulations. A total of 118 data points were collected along the time dimension with an increment of 32 ns. Depending on the sample quality, 30–150 scans were accumulated.

Q-band PELDOR

PELDOR measurements at Q-band frequencies (≈34 GHz) were performed on a Bruker E580 spectrometer equipped with a

dielectric EN 5170 D2 ENDOR probehead. A Bruker AmpQ 10 W solid-state amplifier was used for microwave amplification. Temperature settings were identical to X-band PELDOR measurements. The pump pulse was chosen to coincide with the maximum of the echo-detected field-swept spectrum. Detection was performed at a frequency offset of $\Delta\nu = \nu_A - \nu_B = -50$ MHz (Supplemental Fig. S4B contains a simulated echo-detected field-swept spectrum with visualized pump/probe positions and pulse excitation profiles). Detection pulses had a length of 32 ns, pump pulses were optimized for a length of 21 ns. Tau values of $\tau_1 = 130$ ns and $\tau_2 = 5000$ ns were used. The shot repetition time was set to 7 µs. A tau averaging cycle of 8 × 16 ns was used in order to suppress deuterium modulations. A total of 310 data points were collected along the time dimension with an increment of 16 ns. Depending on the sample quality, 10–50 scans were accumulated. For both, X-band and Q-band measurements, primary PELDOR data were background-corrected by fitting an exponential decay function assuming a homogeneous spatial distribution of the nucleic acid molecules. Tikhonov regularization was performed on background-corrected PELDOR data to obtain the distance probability function $P(r)$. Data processing was done using the Matlab toolbox *DeerAnalysis* (Jeschke et al. 2006).

SUPPLEMENTAL MATERIAL

Supplemental material is available for this article.

ACKNOWLEDGMENTS

We thank Dr. Alice Bowen and Dr. Philipp Spindler for help in setting up initial Q-band and X-band PELDOR measurements. We also thank Dr. Claudia Grytz, Nicole Erlenbach, and Dr. Andriy Marko for help with PELDOR X-band simulations. S.Th.S. acknowledges financial support from the Icelandic Research Fund (141062-051). T.F.P., B.S., and J.E.W. acknowledge financial support from the Collaborative Research Center 902 – Molecular Principles of RNA-based regulation of the German Research Foundation (3214020004).

Received September 6, 2018; accepted October 16, 2018.

REFERENCES

Abé C, Klose D, Dietrich F, Ziegler WH, Polyhach Y, Jeschke G, Steinhoff HJ. 2012. Orientation selective DEER measurements on vinculin tail at X-band frequencies reveal spin label orientations. *J Magn Reson* **216:** 53–61. doi:10.1016/j.jmr.2011.12.024

Berens C, Thain A, Schroeder R. 2001. A tetracycline-binding RNA aptamer. *Bioorg Med Chem* **9:** 2549–2556. doi:10.1016/S0968-0896(01)00063-3

Berens C, Groher F, Suess B. 2015. RNA aptamers as genetic control devices: the potential of riboswitches as synthetic elements for regulating gene expression. *Biotechnol J* **10:** 246–257. doi:10.1002/biot.201300498

Breaker RR. 2012. Riboswitches and the RNA world. *Cold Spring Harb Perspect Biol* **4:** a003566. doi:10.1101/cshperspect.a003566

Chopra I, Roberts M. 2001. Tetracycline antibiotics: mode of action, applications, molecular biology, and epidemiology of bacterial resistance. *Microbiol Mol Biol Rev* **65:** 232–260. doi:10.1128/MMBR.65.2.232-260.2001

Förster U, Weigand JE, Trojanowski P, Suess B, Wachtveitl J. 2012. Conformational dynamics of the tetracycline-binding aptamer. *Nucleic Acids Res* **40:** 1807–1817. doi:10.1093/nar/gkr835

Groher F, Suess B. 2014. Synthetic riboswitches—a tool comes of age. *Biochim Biophys Acta* **1839:** 964–973. doi:10.1016/j.bbagrm.2014.05.005

Gruber AR, Lorenz R, Bernhart SH, Neuböck R, Hofacker IL. 2008. The Vienna RNA websuite. *Nucleic Acids Res* **36:** W70–W74. doi:10.1093/nar/gkn188

Grytz CM, Marko A, Cekan P, Sigurdsson ST, Prisner TF. 2016. Flexibility and conformation of the cocaine aptamer studied by PELDOR. *Phys Chem Chem Phys* **18:** 2993–3002. doi:10.1039/C5CP06158J

Grytz CM, Kazemi S, Marko A, Cekan P, Güntert P, Sigurdsson ST, Prisner TF. 2017. Determination of helix orientations in a flexible DNA by multi-frequency EPR spectroscopy. *Phys Chem Chem Phys* **19:** 29801–29811. doi:10.1039/C7CP04997H

Hallberg ZF, Su Y, Kitto RZ, Hammond MC. 2017. Engineering and in vivo applications of riboswitches. *Annu Rev Biochem* **86:** 515–539. doi:10.1146/annurev-biochem-060815-014628

Hanson S, Berthelot K, Fink B, McCarthy JEG, Suess B. 2003. Tetracycline-aptamer-mediated translational regulation in yeast. *Mol Microbiol* **49:** 1627–1637. doi:10.1046/j.1365-2958.2003.03656.x

Hanson S, Bauer G, Fink B, Suess B. 2005. Molecular analysis of a synthetic tetracycline-binding riboswitch. *RNA* **11:** 503–511. doi:10.1261/rna.7251305

Höbartner C, Sicoli G, Wachowius F, Gophane DB, Sigurdsson ST. 2012. Synthesis and characterization of RNA containing a rigid and nonperturbing cytidine-derived spin label. *J Org Chem* **77:** 7749–7754. doi:10.1021/jo301227w

Jeschke G, Chechik V, Ionita P, Godt A, Zimmermann H, Banham J, Timmel CR, Hilger D, Jung H. 2006. DeerAnalysis2006—a comprehensive software package for analyzing pulsed ELDOR data. *Appl Magn Reson* **30:** 473–498. doi:10.1007/BF03166213

Kötter P, Weigand JE, Meyer B, Entian KD, Suess B. 2009. A fast and efficient translational control system for conditional expression of yeast genes. *Nucleic Acids Res* **37:** e120. doi:10.1093/nar/gkp578

Krstić I, Hänsel R, Romainczyk O, Engels JW, Dötsch V, Prisner TF. 2011. Long-range distance measurements on nucleic acids in cells by pulsed EPR spectroscopy. *Angew Chem Int Ed Engl* **50:** 5070–5074. doi:10.1002/anie.201100886

Larsen RG, Singel DJ. 1993. Double electron–electron resonance spin–echo modulation: spectroscopic measurement of electron spin pair separations in orientationally disordered solids. *J Chem Phys* **98:** 5134–5146. doi:10.1063/1.464916

Marko A, Prisner TF. 2013. An algorithm to analyze PELDOR data of rigid spin label pairs. *Phys Chem Chem Phys* **15:** 619–627. doi:10.1039/C2CP42942J

McCown PJ, Corbino KA, Stav S, Sherlock ME, Breaker RR. 2017. Riboswitch diversity and distribution. *RNA* **23:** 995–1011. doi:10.1261/rna.061234.117

Mignon P, Loverix S, Steyaert J, Geerlings P. 2005. Influence of the π–π interaction on the hydrogen bonding capacity of stacked DNA/RNA bases. *Nucleic Acids Res* **33:** 1779–1789. doi:10.1093/nar/gki317

Milov AD, Salikhov KM, Shchirov MD. 1981. Use of the double resonance in electron spin echo method for the study of paramagnetic center spatial distribution in solids. *Fiz Tverd Tela* **23:** 975–982.

Müller M, Weigand JE, Weichenrieder O, Suess B. 2006. Thermodynamic characterization of an engineered tetracycline-binding riboswitch. *Nucleic Acids Res* **34:** 2607–2617. doi:10.1093/nar/gkl347

Nelson JA, Uhlenbeck OC. 2006. When to believe what you see. *Mol Cell* **23:** 447–450. doi:10.1016/j.molcel.2006.08.001

Pannier M, Veit S, Godt A, Jeschke G, Spiess H. 2000. Dead-time free measurement of dipole–dipole interactions between electron spins. *J Magn Reson* **142:** 331–340. doi:10.1006/jmre.1999.1944

Piton N, Mu Y, Stock G, Prisner TF, Schiemann O, Engels JW. 2007. Base-specific spin-labeling of RNA for structure determination. *Nucleic Acids Res* **35:** 3128–3143. doi:10.1093/nar/gkm169

Prisner TF, Marko A, Sigurdsson ST. 2015. Conformational dynamics of nucleic acid molecules studied by PELDOR spectroscopy with rigid spin labels. *J Magn Reson* **252:** 187–198. doi:10.1016/j.jmr.2014.12.008

Reuss AJ, Vogel M, Weigand JE, Suess B, Wachtveitl J. 2014. Tetracycline determines the conformation of its aptamer at physiological magnesium concentrations. *Biophys J* **107:** 2962–2971. doi:10.1016/j.bpj.2014.11.001

Saris NE, Mervaala E, Karppanen H, Khawaja JA, Lewenstam A. 2000. Magnesium—an update on physiological, clinical and analytical aspects. *Clin Chim Acta* **294:** 1–26. doi:10.1016/S0009-8981(99)00258-2

Suess B, Hanson S, Berens C, Fink B, Schroeder R, Hillen W. 2003. Conditional gene expression by controlling translation with tetracycline-binding aptamers. *Nucleic Acids Res* **31:** 1853–1858. doi:10.1093/nar/gkg285

Tkach I, Pornsuwan S, Höbartner C, Wachowius F, Sigurdsson ST, Baranova TY, Diederichsen U, Sicoli G, Bennati M. 2013. Orientation selection in distance measurements between nitroxide spin labels at 94 GHz EPR with variable dual frequency irradiation. *Phys Chem Chem Phys* **15:** 3433. doi:10.1039/c3cp44415e

Vogel M, Suess B. 2016. Label-free determination of the dissociation constant of small molecule-aptamer interaction by isothermal titration calorimetry. *Methods Mol Biol* **1380:** 113–125. doi:10.1007/978-1-4939-3197-2_9

Vogel M, Weigand JE, Kluge B, Grez M, Suess B. 2018. A small, portable RNA device for the control of exon skipping in mammalian cells. *Nucleic Acids Res* **46:** e48. doi:10.1093/nar/gky062

von Hagens T, Polyhach Y, Sajid M, Godt A, Jeschke G. 2013. Suppression of ghost distances in multiple-spin double electron–electron resonance. *Phys Chem Chem Phys* **15:** 5854–5866. doi:10.1039/c3cp44462g

Weigand JE, Suess B. 2007. Tetracycline aptamer-controlled regulation of pre-mRNA splicing in yeast. *Nucleic Acids Res* **35:** 4179–4185. doi:10.1093/nar/gkm425

Weinrich T, Jaumann EA, Scheffer U, Prisner TF, Göbel MW. 2018. A cytidine phosphoramidite with protected nitroxide spin label: synthesis of a full-length TAR RNA and investigation by in-line probing and EPR spectroscopy. *Chemistry* **24:** 6202–6207. doi:10.1002/chem.201800167

Wunnicke D, Strohbach D, Weigand JE, Appel B, Feresin E, Suess B, Müller S, Steinhoff HJ. 2011. Ligand-induced conformational capture of a synthetic tetracycline riboswitch revealed by pulse EPR. *RNA* **17:** 182–188. doi:10.1261/rna.2222811

Xiao H, Edwards TE, Ferré-D'Amaré AR. 2008. Structural basis for specific, high-affinity tetracycline binding by an in vitro evolved aptamer and artificial riboswitch. *Chem Biol* **15:** 1125–1137. doi:10.1016/j.chembiol.2008.09.004

Influence of Mg^{2+} on the conformational flexibility of a tetracycline aptamer

Thilo Hetzke, Marc Vogel, Dnyaneshwar B. Gophane, et al.

RNA 2019 25: 158-167 originally published online October 18, 2018
Access the most recent version at doi:10.1261/rna.068684.118